Geophysical Journal International

Geophys. J. Int. (2015) **203,** 664–677 doi: 10.1093/gji/ggv302
GJI Seismology

Effect of off-fault low-velocity elastic inclusions on supershear rupture dynamics

Xiao Ma and A.E. Elbanna

Department of Civil and Environmental Engineering, University of Illinois at Urbana-Champaign, Urbana, IL 61801*, USA. E-mail: xiaoma5@illinois.edu; elbanna2@illinois.edu*

Accepted 2015 July 15. Received 2015 July 14; in original form 2015 April 27

SUMMARY

Heterogeneous velocity structures are expected to affect fault rupture dynamics. To quantitatively evaluate some of these effects, we examine a model of dynamic rupture on a frictional fault embedded in an elastic full space, governed by plane strain elasticity, with a pair of off-fault inclusions that have a lower rigidity than the background medium. We solve the elastodynamic problem using the Finite Element software Pylith. The fault operates under linear slip-weakening friction law. We initiate the rupture by artificially overstressing a localized region near the left edge of the fault. We primarily consider embedded soft inclusions with 20 per cent reduction in both the pressure wave and shear wave speeds. The embedded inclusions are placed at different distances from the fault surface and have different sizes. We show that the existence of a soft inclusion may significantly shorten the transition length to supershear propagation through the Burridge-Andrews mechanism. We also observe that supershear rupture is generated at pre-stress values that are lower than what is theoretically predicted for a homogeneous medium. We discuss the implications of our results for dynamic rupture propagation in complex velocity structures as well as supershear propagation on understressed faults.

Key words: Earthquake dynamics; Wave propagation.

1 INTRODUCTION

The velocity structure in the vicinity of pre-existing fault networks is, in general, heterogeneous (SCEDC 2013). In particular, faults zones are typically composed of rocks and granular materials that have experienced different cycles of damage and healing. This leads to time-dependent variations in the magnitude of elastic moduli and the wave speeds (Ben-Zion & Sammis 2003). The existence of heterogeneities is expected to affect rupture propagation on the embedded fault segments due to wave reflection, transmission and diffraction from the boundaries of these inclusions.

Of the different complexities that may arise in the velocity structure near pre-existing faults, the properties of low-velocity zones (LVZs) have been extensively studied. Examples include LVZs around San Andreas (Li & Leary 1990; Li *et al.* 2006; Lewis & Ben-Zion 2010), San Jacinto (Lewis *et al.* 2005; Yang & Zhu 2010), Landers (Li *et al.* 1994; Peng *et al.* 2003; Li *et al.* 2007), Hector Mine (Li *et al.* 2002), Calico (Cochran *et al.* 2009; Yang *et al.* 2011), Nojima (Mizuno *et al.* 2008), and North Anatolian (Ben-Zion *et al.* 2003) fault zones.

The implications of the existence of an LVZ adjacent to the fault surface, within an otherwise homogeneous medium, have been explored using spontaneous dynamic rupture models (Archuleta & Day 1980; Harris & Day 1997; Ben-Zion & Huang 2002; Huang & Ampuero 2011; Huang *et al.* 2014). The velocity reduction within the LVZ, relative to the country rock, may vary in the range of 20–60 per cent (Huang & Ampuero 2011). It was found that the trapped waves in the LVZ alter the shear stress on the fault plane and affect both the dynamic rupture mode (e.g. Huang & Ampuero 2011) and rupture characteristics including supershear propagation. (Harris & Day 1997; Huang & Ampuero 2011; Huang *et al.* 2014). The enhanced supershear transition observed in simulations with LVZs (Huang *et al.* 2014) suggests that more heterogeneous velocity structures must be considered when investigating rupture speed.

Supershear rupture propagation has been inferred from seismic observations for natural faults in several large strike-slip earthquakes, including the 1979 Imperial Valley earthquake (Archuleta 1984; Spudich & Cranswich 1984), the 1999 Kocaeli (Izmit) earthquake (Bouchon *et al.* 2000, 2001), the 1999 Duzce earthquake (Bouchon *et al.* 2001; Konca *et al.* 2010), the 2001 Kokoxili (Kunlun) earthquake (Bouchon & Vallée 2003; Robinson *et al.* 2006; Vallee *et al.* 2008; Walker & Shearer 2009), the 2002 Denali earthquake (Dunham & Archuleta 2004; Celebi *et al.* 2004), the supershear rupture associated with the aftershock of 2013 Sea of Okhotsk earthquake (Zhan *et al.* 2014).

The transition from a rupture velocity less than the Rayleigh velocity to a rupture velocity greater than the shear wave velocity has been studied using dynamic rupture simulations (Burridge 1973; Andrews 1976; Das & Aki 1977; Day 1982; Madariaga & Olsen 2000; Ben-Zion & Huang 2002; Fukuyama & Olsen 2002;

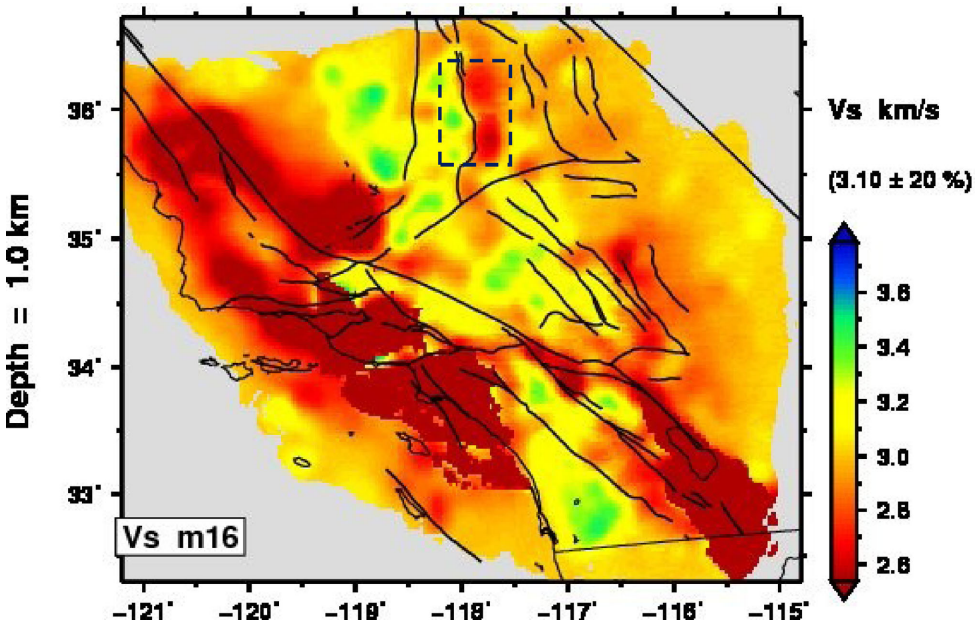

Figure 1. Material variation across the horizontal cross section in the earth (Carl Tape 2009). An example of a velocity structure similar to our investigation (e.g. an off-fault low-velocity inclusion) is highlighted within the dashed rectangle.

Festa & Vilotte 2006; Dunham 2007; Liu & Lapusta 2008; Oglesby *et al.* 2008; Shi *et al.* 2008; Lapusta & Liu 2009; Daub *et al.* 2010; Kaneko & Lapusta 2010; Bizzarri 2012; Bizzarri & Das 2012; Elkhoury & Knopoff 2012; Gabriel *et al.* 2012; Langer *et al.* 2012; Le Goff *et al.* 2013; Huang *et al.* 2014; Ryan & Oglesby 2014). The primary mechanism for the supershear transition is known as the Burridge-Andrews mechanism (Burridge 1973; Andrews 1976), occurring when a daughter crack is nucleated at the *S*-wave shear stress peak ahead of the propagating Mode II rupture.

In order for the Burridge–Andrews mechanism to take place on a homogeneous fault in 2-D models, the pre-stress must be high enough. The strength parameter S (Andrews 1976; Das & Aki 1977), which is given by the difference between the static shear strength and initial stress divided by the difference between the initial stress and the dynamic strength, has to be smaller than a critical value of $S_{crit} = 1.77$. Previous work has shown that heterogeneities on the fault surface, including variations in the pre-stress or fracture energy (Dunham *et al.* 2003; Liu & Lapusta 2008), may enable supershear propagation at lower pre-stress values than what are theoretically predicted under homogeneous conditions. The effect of off-fault heterogeneities in the form of off-fault plasticity and damage has also been recently investigated (Huang *et al.* 2014). The influence of off-fault material heterogeneities, as may be represented by inclusions or layered structure, is the focus of this paper.

Material gradient and contrasts may not be confined to the vicinity of fault surfaces. Velocity anomalies in the form of lenses with lower or higher wave speeds than the surrounding medium may exist at some distance from the fault surface (Fig. 1). In this case, additional interfaces, introduced by the boundaries of the domain with the different rigidity, produce multiple reflections in the wavefield as well as diffraction and refraction effects. These modulations may influence the rupture process and increase the complexity of the dynamic response. In this paper we model dynamic rupture propagation on a slip-weakening fault in an elastic domain with an embedded inclusion of a lower rigidity. This softer inclusion may not be directly adjacent to the fault surface and it may have a limited extension relative to the fault length. It may be taken as an analogue of a sedimentary basin or a zone that is heavily damaged relative to its surroundings. Section 2 describes the model setup and parameters selection. In Section 3, we show the simulation results regarding the influence of the embedded soft inclusion on the supershear transition as well as rupture propagation characteristics. We examine the robustness of our findings with respect to variations in the soft inclusion thickness, the off-fault distance, material contrast degree, and the stress level effect. In Section 4, we discuss the implications of our results in the context of other observational and computational models involving LVZs and supershear ruptures. We summarize our conclusions in Section 5.

2 MODEL SETUP

We consider a planar fault in a linear elastic isotropic medium under inplane strain conditions. The medium has a shear modulus μ_1 everywhere except for the inclusion that possesses a smaller shear modulus μ_2. The inclusion geometry is idealized as a rectangular domain with a width H_2, a length H_3, and is located at a distance H_1 from the fault. We shifted the inclusion by a distance H_4 in the horizontal direction to ensure that the rigidity around the nucleation patch is not affected by the inclusion. The medium geometry is symmetric about the fault plane (Fig. 2). Absorbing boundary conditions are applied at the four boundaries of the domain to mimic an infinite extension in all direction. In this study we assume the inclusion pair to be symmetric about the fault plane. By setting up such geometry we focus our study on the supershear rupture induced by the dynamic shear stress while keeping the normal stress along the fault at its static value.

The fault friction is governed by linear slip-weakening law (Ida 1972; Palmer & Rice 1973), where the frictional shear strength Γ decreases linearly as a function of slip δ from its static value τ_s to the dynamic value τ_d over a characteristic slip d_c (eq. 1). We keep the friction law parameters the same in all our simulations. We choose the static friction coefficient to be 0.6, the dynamic friction

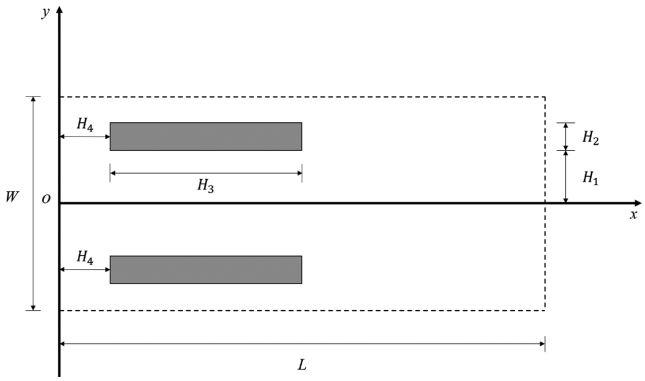

Figure 2. The model geometry. The simulated domain has an aspect ratio of L/W. A slip-weakening fault of length L bisects the domain and acts as a horizontal symmetry line. Light grey layers represent the location of the soft inclusions. H_1 defines the distance between the fault and the material boundary. H_2 defines the thickness of the soft layer. H_3 defines the length of the soft layer. H_4 defines the off-edge distance of the soft layer inclusion. In most cases investigated here we set $H_4 = 10$ km. Absorbing boundary conditions are used for all edges to simulate an infinite extension in all directions.

coefficients to be 0.5, and the characteristic slip-weakening distance to be 0.2 m:

$$\Gamma(\delta) = \begin{cases} \tau_d + (\tau_s - \tau_d)(1 - \delta/d_c), & \delta \leq d_c \\ \tau_d, & \delta > d_c \end{cases}. \quad (1)$$

The static strength τ_s and the dynamic strength τ_d are the products of the effective normal stress and the corresponding static and dynamic friction coefficients, respectively. We discuss the implications of the choice of this particular friction law compared to other formulations, such as rate and state friction, in Section 4.

We solve the dynamic rupture problem under 2-D plane strain conditions using the finite element program Pylith (Aagaard *et al.* 2013). A uniform mesh with a 25 m grid size has been found to be adequate for resolving the process zone within the range of parameter values explored in this study. We conduct a mesh convergence study with 12.5 m element sizes in Appendix A. The results are not affected by the mesh refinement.

Table 1 summarizes the different parameter values. The fundamental length scale in this problem is given by eq. (2):

$$R = \frac{\mu_1 d_c}{(\tau_s - \tau_d)}, \quad (2)$$

where μ_1 is the shear modulus of the homogeneous domain, d_c is the slip-weakening distance, τ_s and τ_d are the static and dynamic shear strength values, respectively. This length scale R is proportional to the universal nucleation length predicted for linear slip-weakening friction (Uenishi & Rice 2003) in a homogeneous medium with a shear modulus μ_1.

To start the dynamic rupture, we overstress the fault beyond its static frictional strength in a limited region extending for a distance equal to R to ensure the immediate dynamic propagation. The nucleation procedure is depicted in Appendix B. In previous studies, it was pointed out that the nucleation procedure may affect the subsequent dynamic rupture evolution (Festa & Vilotte 2006; Shi *et al.* 2008; Payne & Duan 2015). We use the same nucleation procedure in all simulations. We discuss the implications of the abrupt nucleation adopted here as compared to other nucleation procedures—including quasi-static nucleation—in Section 4.

3 RESULTS

In this section, we investigate the influence of the existence of an off-fault low-velocity lens on the rupture mode and transition to supershear.

3.1 Supershear rupture propagation in the presence of off-fault low-velocity inclusion

The existence of an off-fault heterogeneity with a lower shear modulus than the surrounding bulk enriches the wavefield by introducing additional boundary surfaces. The waves emanating from the rupture and propagating through the heterogeneous medium are modulated by the reflection and the refraction at the different material interfaces. These modulations include changes in wave amplitudes, phase angles, and polarities. In Fig. 3, we plot the reflection coefficient for the P and SV waves at both the lower and upper boundaries

Table 1. Model discretization and constitutive parameters.

Medium and discretization parameters	Value
Shear modulus of the background domain	32 GPa
S-wave velocity (background), c_s	3.464 km s^{-1}
P-wave velocity (background), c_p	6.0 km s^{-1}
Mass density for all layers, ρ	2670 kg m^{-3}
Fault length, L	100 km
Domain width, W	30 km
Fault	$\{x, y \vert y = 0, 0 < x < 100 \text{ km}\}$
Overstress region on the fault	$\{x, y \vert y = 0, 0 < x < 1.2 \text{ km}\}$
Spatial grid space $\Delta x = \Delta y$	25 m
Wave velocity contrast	20 per cent
Fault constitutive parameters	**Value**
Magnitude of the effective normal stress, σ_n^{eff}	50.0 MPa
Overstressed region initial shear stress	31.0 MPa
Static friction coefficient, μ_s	0.6
Dynamic friction coefficient, μ_d	0.5
Static strength, τ_s	30.0 MPa
Dynamic strength, τ_d	25.0 MPa
Strength parameter, S	Varies
Characteristic slip-weakening distance, d_c	0.2 m

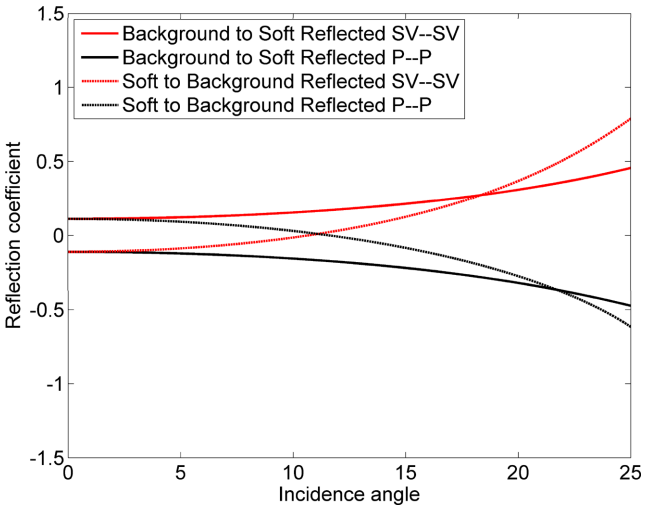

Figure 3. Reflection coeficient for incidient *SV*, *P* waves at boundary between background medium and soft layer with velcoity reduction of 20 per cent, the filled line shows the incident wave background medium to soft layer and the dot line shows the incident wave from soft layer to background medium, respectively. The reflected *SV*, *P* waves are considered. The incident angles of *SV*, *P* waves are plotted below the first critical angle. The phase is zero for this range of incident angles. Formulas of reflection coefficients are taken from Aki & Richards (2002).

of a hypothetical soft layer for the case corresponding to a mismatch in *P*-wave speed = 20 per cent. We consider different values of the incidence angle. For *SV*–*SV* ray, waves reflected from the lower boundary of the soft layer have the same polarity as the incident wave for the whole range of incidence angles considered here. Thus, these waves enhance the rupture propagation. On the other hand, the waves reflected from the upper boundary of the soft layer have negative reflection coefficients for incidence angles less than 10°. When these waves are transmitted back to the fault zone, their reversed polarity impedes the rupture and may lead to temporary rupture arrest and formation of slip pulses as we will discuss shortly. For the *P*–*P* ray, waves reflected from the lower boundary of the soft layer have reversed polarity for the full considered range of incidence angles while the waves reflected from the upper boundary of the soft layer have positive reflection coefficients for incidence angles smaller than 10°. However, due to the symmetry, the normal stress on the fault remains unaltered. This scenario, particularly for the *SV* waves, differs from when the low-velocity layer is adjacent to the fault plane. In this case, only reflections from the far-side layer boundary are present leading to rupture decoherence (Huang & Ampuero 2011; Huang *et al.* 2014).

We first consider a fault case with strength parameter $S = 1$. In a homogeneous medium, we observe that the rupture jumps into supershear after propagating for a distance ∼65.25 km.

The existence of the soft heterogeneity reduces the supershear transition distance. The extent of the effect depends on many factors such as the soft inclusion thickness, the soft inclusion extension, the soft inclusion distance from the fault, and the velocity reduction in the soft inclusion. These factors determine the amplitudes of the waves reflected from the soft layer to the fault zone as well as the perturbations in the nucleation size of the daughter crack. In particular, the width of the soft inclusion determines the difference in arrival times, as observed on the fault surface, between the different waves reflected from the two boundaries of the soft layer. For a soft inclusion of length 10 km and width $H_2 = 2R$, where R is the nucleation length, the transition distance to supershear is reduced to only 14.55 km compared to 65.25 km for the homogeneous case. This reduction may be attributed to two reasons. First, the shear waves reflected from the near-side boundary of the soft inclusion have the same polarity as the incident wave, and thus, they enhance the rupture propagation. This thickness of the soft inclusion $H_2 = 2R$ is big enough to delay the arrival of the reflected waves from the far-side boundary. Since these waves have an opposite polarity they interfere destructively with the rupture. When the soft inclusion thickness is smaller (e.g. $H_2 = R$) these waves arrive sooner to the fault surface and compete with the enhanced effect carried by the reflected waves from the near-side boundary. In this case, the transition distance is close to its value in the homogeneous case.

The second reason is that the nucleation length for a crack is proportional to the rigidity of the domain (eq. 2). The existence of a soft inclusion reduces the local effective rigidity of the medium compared to the homogeneous case. Thus the nucleation size of the daughter crack will be smaller in the presence of a soft inclusion. This is shown in Fig. 4. There, we track the width of the region for which the peak shear stress is equal to the static strength. We define the nucleation size of the daughter crack as the size of this region just before it becomes disjoint. Based on this definition, we have found that the nucleation length of the daughter crack is reduced from 300 m, for the homogeneous medium, to 200 m, for the case with softer inclusion. The nucleation size of the daughter crack is smaller than what is predicted for quasi-static nucleation (eq. 1). This is because the nucleation of the daughter crack is enhanced by the dynamic stress field of the primary crack.

Fig. 5 shows the variation of the rupture speed for the homogeneous and heterogeneous cases. We compute the rupture speed by recording the location of the rupture tip at each time step. To eliminate numerical artefacts associated with the finite space–time discretization, we fit the tip position–time curve with a polynomial of degree 9. By differentiating the smoother curve that resulted from the fitting process, the instantaneous rupture tip speed is computed, as shown in Fig. 5. We have also depicted the shear wave speed as well as the Rayleigh wave speed for the fault zone material on the same plot.

In both cases, the supershear transition occurs discontinuously through the nucleation of a daughter crack as predicted by the Burridge–Andrews mechanism. The discontinuity in the rupture speed plot corresponds to the nucleation of the supershear tip. For the homogeneous case, the supershear rupture transition occurs at 65.25 km, whereas for the soft layer case the supershear transition happens at approximately 14.55 km. In both cases prior to the supershear jump, the rupture travels at sub-Rayleigh wave speed. There is no propagation through the so called ‘Energetically Forbidden Zone’ defined by the range of velocities between the shear wave and Rayleigh wave speed (Freund 1990).

Another feature of the rupture speed plot (Fig. 5) is the existence of a dip shortly after the transition to supershear. This is related to the details of the supershear transition process. Shortly after it is formed, the daughter crack joins the main rupture, and the leading rupture tip propagates at supershear velocity while the main rupture tip is still propagating at lower velocity. As a result, the distance between the leading edge and the main rupture front continues to increase eventually leading to the detachment of a supershear pulse. This mechanism occurs in both the homogeneous and layered cases (Fig. 5). After the detachment, the rupture propagation speed of the slip pulse increases until it saturates at a speed between $\sqrt{2}c_s$ and c_p of the fault zone (Dunham & Archuleta 2004).

Fig. 6 shows the space–time evolution of the slip rate on the fault surface in the two cases. For the case of homogeneous medium the

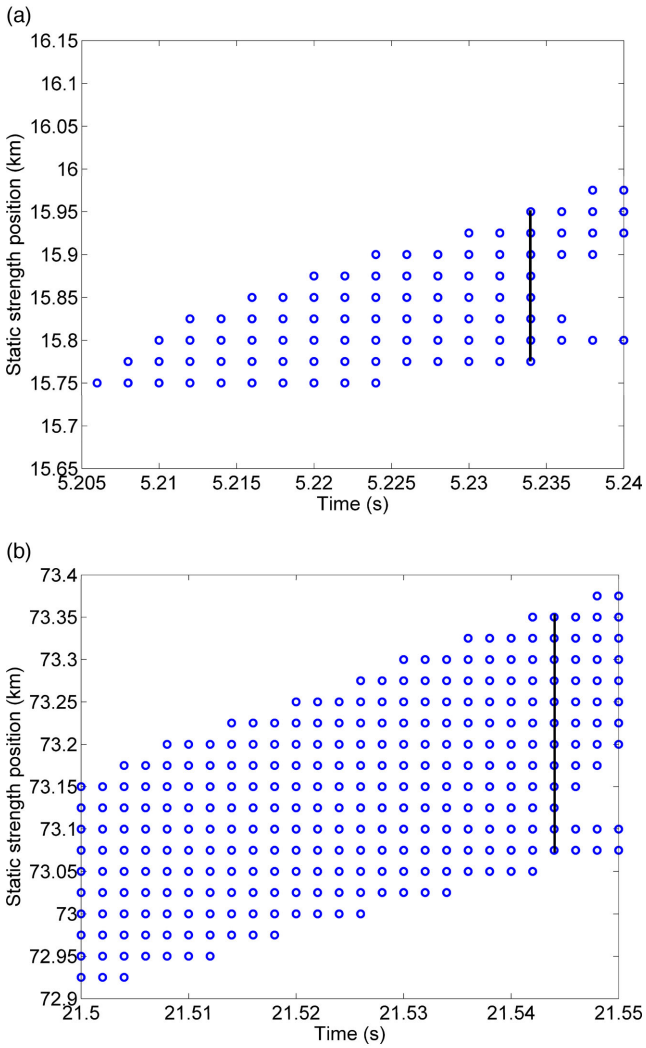

Figure 4. Growth of the daughter crack in the presence (a) and absence (b) of soft inclusion. Here the location of the fault points where the shear stress is equal to the static frictional stress (30 MPa) is plotted. The nucleation length (marked with the black bar) of the daughter crack in the soft layer inclusion case is 200 m while in the homogeneous case is 300 m. Simulation parameters: (a) ($H_1 = R$, $H_2 = 2R$, $H_3 = 20$ km, $H_4 = 10$ km, material contrast = 20 per cent, $R = 1.2$ km, $S = 1.0$); (b) homogeneous domain ($H_1 = 0$, $H_2 = 0$, $H_3 = 0$, $H_4 = 0$, material contrast = 0 per cent, $R = 1.2$ km, $S = 1.0$).

slip rate is smoother. The multiple reflections from the different interfaces in the medium with an LVZ lead to oscillations in the slip rate. Depending on the material contrast, these oscillations may become large enough to lead to the temporary arrest of the rupture behind the leading edge and the formation of a train of pulses (not shown here).

Fig. 7 shows the evolution of maximum slip rate for both the homogeneous and inhomogeneous media. The existence of the embedded soft inclusion leads to the saturation of the maximum slip rate of 2.0 m s^{-1} during the sub-Rayleigh propagation. After the supershear jump, and as the rupture propagates into the homogeneous medium, the maximum slip rate starts to increase again. In the homogeneous case, on the other hand, the maximum slip rate increase monotonically up to 10 m s^{-1} in the sub-Rayleigh regime. The sudden jump in the maximum slip rate profile in both cases point to the supershear transition. The end of the drop following

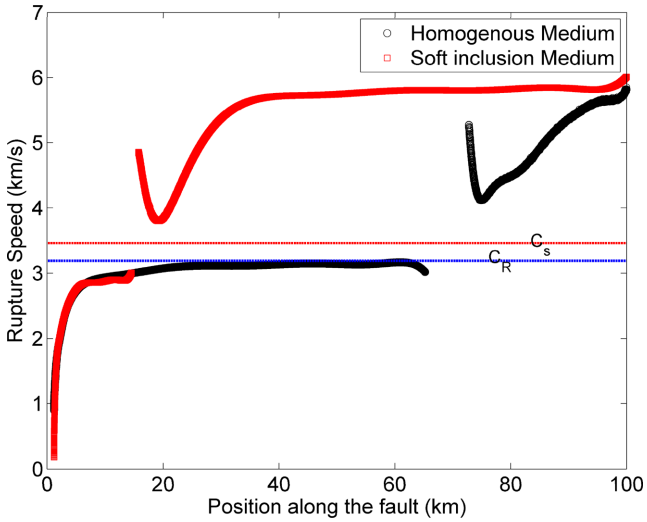

Figure 5. Variation of rupture speed for homogeneous medium and medium with soft layer inclusion. The jump represents the nucleation of daughter crack through the Burridge–Andrews mechanism. The dip after the jump represents the detachment of the supershear pulse. The nucleation of daughter crack for the case of homogeneous medium occurs at 65.25 km; for case of medium with soft layer inclusion, the nucleation of daughte crack occurs at 14.55 km. c_s represents the shear wave speed and c_R represents the Rayleigh wave speed. Simulation parameters: ($H_1 = R$, $H_2 = 2R$, $H_3 = 10$ km, $H_4 = 10$ km, material contrast = 20 per cent, $R = 1.2$ km, $S = 1.0$).

this jump refers to the detachment of supershear slip pulse. These observations suggest that the presence of a soft inclusion leads to the occurrence of supershear transition at lower smaller slip values than in the homogeneous case. Also the magnitude of the maximum slip rate is smaller in the soft layer case than the homogeneous case even though the rupture propagates faster in the former than in the latter. The same observation applies to the rate of change of the maximum slip rate. Although both tips are propagating in the same homogeneous medium (after the soft inclusion ends), the maximum slip rate increases at a faster rate in the homogeneous case than in the case with low-velocity lens. This points to the necessity of accounting for the rupture history when estimating rupture quantities such as slip and maximum slip rate.

3.3. Effect of soft inclusion thickness and off-fault distance

In this section, we investigate the effect of soft layer thickness (H_2) and off-fault distance (H_1) on the supershear transition length. For this purpose, we assume that the inclusion extends for the full length of the fault. We normalize these two quantities by R. For $H_2/R = 2$, we vary H_1/R between 1 and 10. As shown in Fig. 8, the more distant the soft layer is from the fault surface, the longer the transition distance to supershear propagation is. On the other hand, for $H_1/R = 1$, we vary H_2/R between 1 and 10. In this case, as the thickness of the soft layer increases, the transition length decreases.

These observations are explained as follows. The shear waves reflected from the far-side and near-side surfaces of the soft layer have opposite polarities (Fig. 3). The traveltime for a ray emanating from the rupture, reflected from one of these interfaces, and arriving back at the fault surface, depends on the layer thickness as well as its distance from the surface. The more distant the soft layer is from the fault surface, the longer this traveltime will be. As a result, there is a

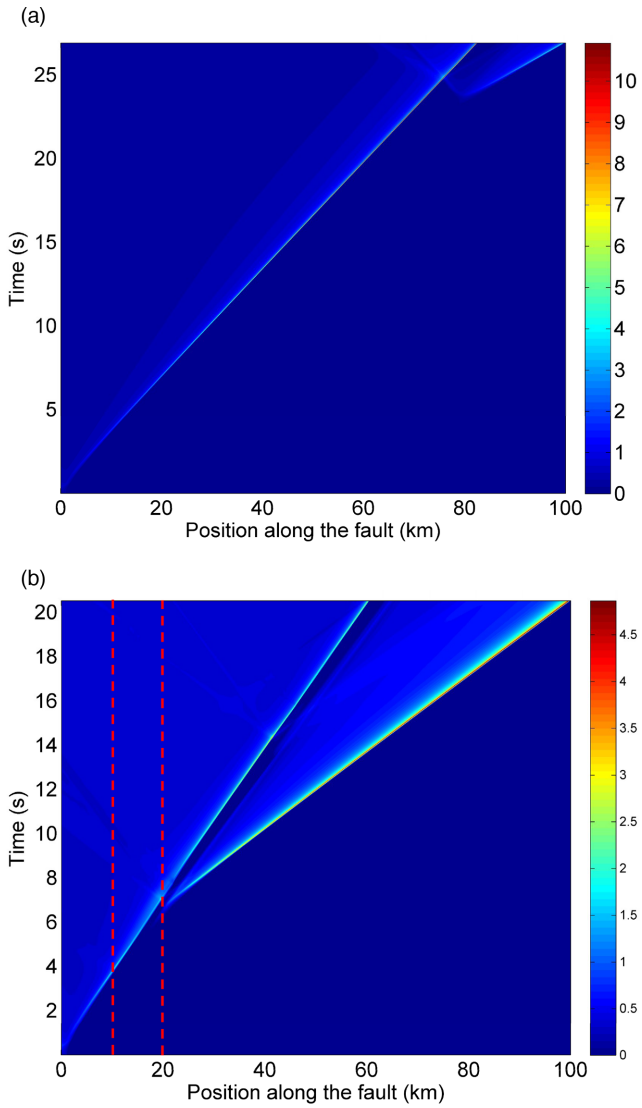

Figure 6. Space-time contours of slip rate on the fault surface (a) homogeneous medium and (b) medium with soft layer inclusion extending 10 km. The red dashed line indicates the location of the soft inclusion. The homogeneous medium has smoother slip rate profile (no oscillations in the slip rate behind the supershear front). Simulation parameters: $H_1 = R$, $H_2 = 2R$, $H_3 = 10$ km, $H_4 = 10$ km, material contrast = 20 per cent, $R = 1.2$ km, $S = 1.0$.

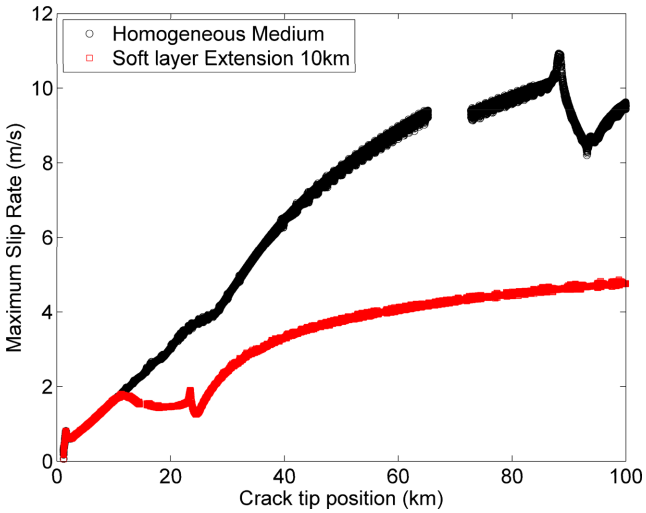

Figure 7. Evolution of maximum slip rate for homogeneous medium and medium with soft layer inclusion extending 10 km. The gap corresponds to the supershear jump. Simulation parameters: $H_1 = R$, $H_2 = 2R$, $H_3 = 10$ km, $H_4 = 10$ km, material contrast = 20 per cent, $R = 1.2$ km, $S = 1.0$.

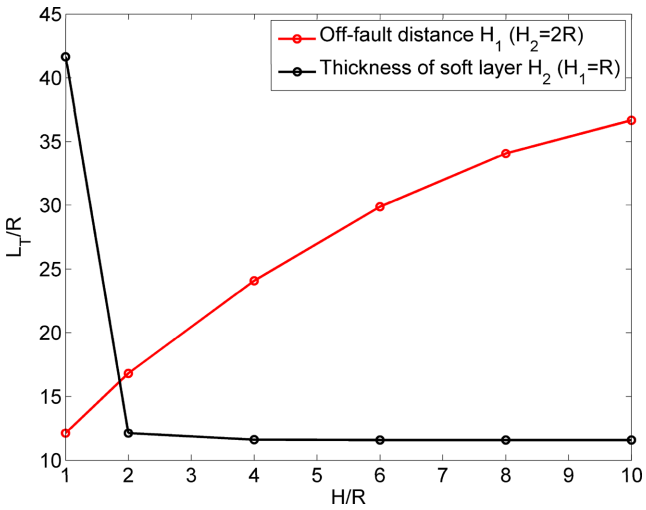

Figure 8. Variation of supershear transition length with different values of off-fault distance (H_1) and soft layer thickness (H_2). With $H_2 = 2R$, red line shows transition length to supershear rupture under various off-fault distance H_1. With $H_1 = R$, black line shows transition length to supershear rupture under various soft layer thicknesses H_2. (Simulation parameters: $H_3 = 90$ km, $H_4 = 10$ km, material contrast = 20 per cent, $R = 1.2$ km, $S = 1.0$.)

delay in the arrival of the waves reflected from the near-side surface. These waves enhance the rupture propagation and accelerate the supershear transition. Their delay increases the transition length.

The increase in the soft layer thickness, on the other hand, enhances the supershear transition and shortens the transition length. As the soft layer thickness increases, the difference in arrival time, as observed at a point on the fault surface, between the waves reflected from the far-side and near-side boundaries of the soft layer increases. The delayed arrival of the waves reflected from the upper boundary reduces their destructive interference effect allowing more time for the rupture to interact with the waves reflected from the near-side boundary. The latter, having the same polarity as the incident waves, enhances the propagation dynamics and accelerates the rupture transition into supershear. This is shown in Fig. 8, where the transition length changes significantly as H_2 changes from R to $2R$ but nearly saturates thereafter. This saturation reflects the observation that increasing the soft layer thickness beyond a certain limit is ineffective in changing the transition length. This is because any further delay in the arrival of the reversed polarity waves from the far-side boundary of the soft layer is irrelevant if the supershear transition has already happened. The trend in Fig. 8 suggests that variations in the distance of the soft layer from the fault surface have a strong impact on the transition length. On the other hand, the effect of the layer thickness is only relevant for a limited range of thickness values. For a given off-fault distance, increasing the layer thickness beyond a certain value has a negligible effect on the supershear transition.

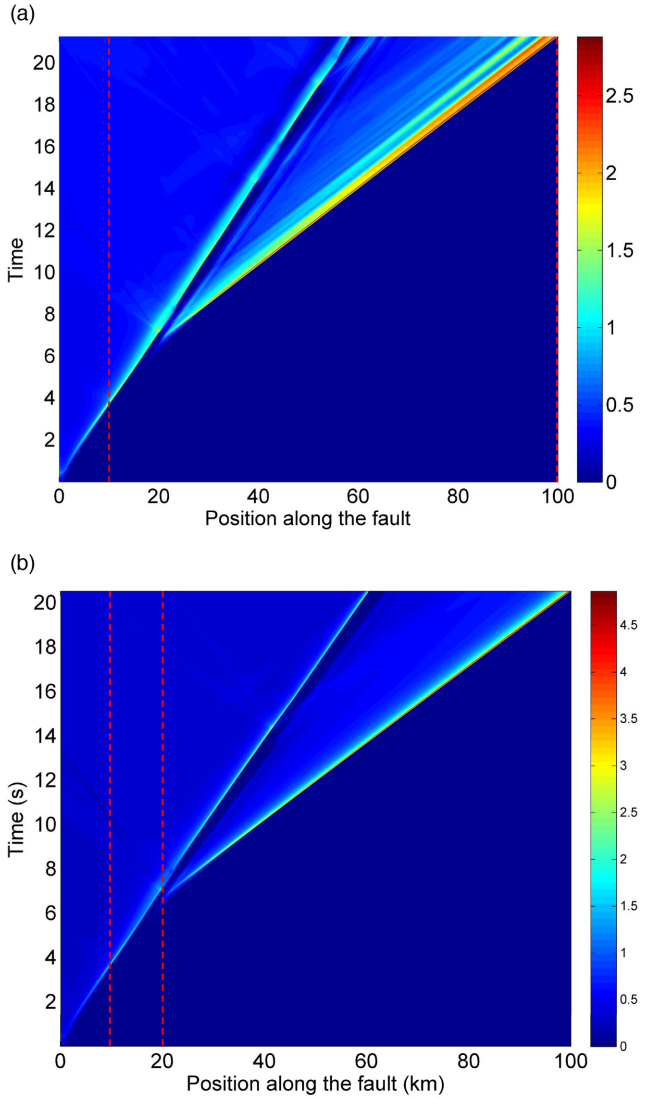

Figure 9. Space–time contour of slip rate during rupture propagations. (a) Soft layer extends to the full length of the domain (100 km) (b) Soft layer extends only 10 km from 10 to 20 km. The red dashed line indicates the location of the soft inclusion. Case (a) exhibits more oscillations in the slip rate profile behind the supershear rupture front. (Simulation parameters: (a) $H_1 = R$, $H_2 = 2R$, $H_3 = 90$ km, $H_4 = 10$ km, material contrast = 20 per cent, $R = 1.2$ km, $S = 1.0$; (b) $H_1 = R$, $H_2 = 2R$, $H_3 = 10$ km, $H_4 = 10$ km, material contrast = 20 per cent, $R = 1.2$ km, $S = 1.0$)

3.4 Effect of soft layer extension

The low-velocity layer may extend to different lengths. Fig. 9 compares snapshots of slip rate in two cases: (1) a soft layer extending full length and (2) a soft layer extending only for 10 km. Both cases have a strength parameter $S = 1$ and a velocity reduction is 20 per cent. For both cases, the supershear transition distance is approximately 14.55 km. This suggests that accelerated supershear transition is insensitive to the length of the soft layer as long as the length of the soft layer is larger than a critical value. This value is set by the velocity contrast and the distance of the soft layer from the fault surface. Moreover, the rupture continues to propagate as supershear into the homogeneous medium after the truncation of the soft layer at 10 km long. We discuss the implications of this on conditions for accelerated supershear transition under heterogeneous conditions in Section 4.

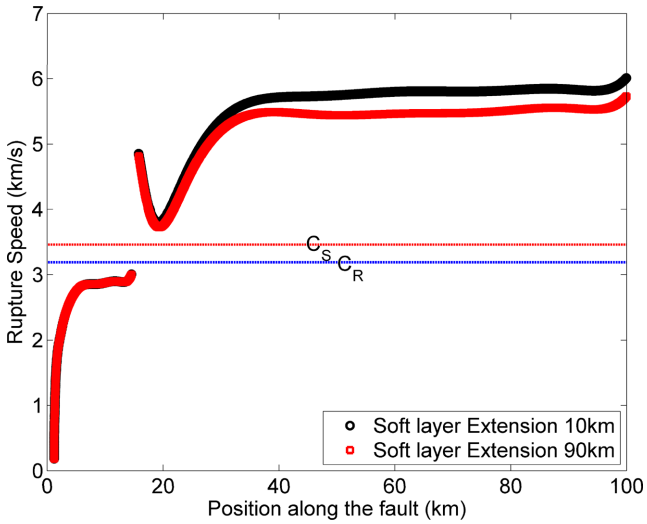

Figure 10. Variation of rupture speed for medium with a case of a medium with soft layer only extending 10 km and a case of soft layer extending full length. The rupture speed is slightly higher for the case with the truncated soft layer. See the text for discussion. c_s represents the shear wave speed and c_R represents the Rayleigh wave speed. (Simulation parameters: black curve: $H_1 = R$, $H_2 = 2R$, $H_3 = 10$ km, $H_4 = 10$ km, material contrast = 20 per cent, $R = 1.2$ km, $S = 1.0$; red curve: $H_1 = R$, $H_2 = 2R$, $H_3 = 90$ km, $H_4 = 10$ km, material contrast = 20 per cent, $R = 1.2$ km, $S = 1.0$.)

However, there are a few differences between the two cases. Most notably, the rupture propagating into the homogeneous medium, after the soft layer is truncated, shows a smoother slip rate profile with no oscillations behind the first rupture front. This is not the case when the soft layer extends to the full length of the fault. In this case, the oscillations in the slip rate are caused by the multiple reflections of the waves from the soft layer boundaries. The truncation of the soft layer eliminates the cause of theses oscillations.

In Fig. 10 we compare the rupture speeds for the two cases. Initially, both ruptures have essentially the same rupture speed. However, the rupture speed is slightly higher for the case of the truncated soft layer. This suggests that wave reflections from the upper boundary of the fully extended soft layer interfere destructively with the wavefield surrounding the crack tip and slightly lower its propagation speed. These reflections are absent in the case of soft layer extending only for 10 km.

In Fig. 11, we compare the evolution of maximum slip rate when the soft layer has a limited extension of 10 km and when it extends to the full length of the fault. The two cases are identical as the rupture tip reaches 23 km. There is a very small difference in the time of supershear transition (see the first peak in the maximum slip rate profile) between the two cases. The supershear transition is slightly delayed in the case of soft layer that is extending for the full length. Also, wave reflections from the boundaries of the soft layer limit the maximum slip after supershear transition to approximately 2.5 m s^{-1}. However, in the case of the 10 km long soft layer, the magnitude of the maximum slip rate increases as the rupture propagates into the homogeneous medium.

To investigate the effect of shorter inclusions, we show in Fig. 12 the evolution of the rupture speed for two cases: a soft layer extending 5 km and a soft layer extending 10 km. The transition length to supershear has increased significantly for the soft layer extending 5 km (∼45.13 km) compared to the one extending for 10 km

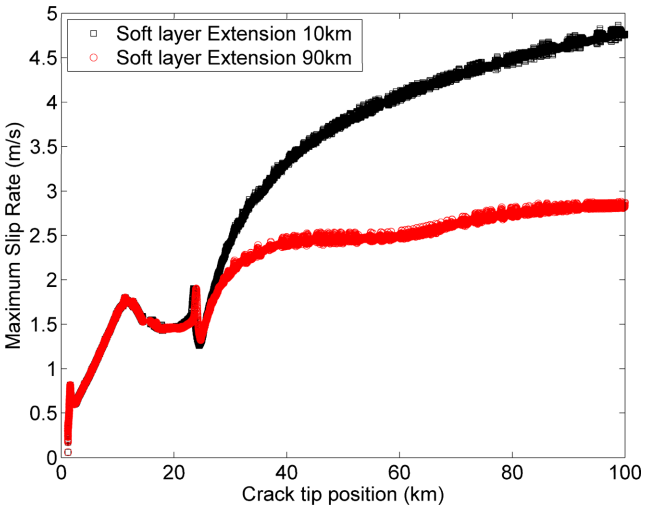

Figure 11. Evolution of maximum slip rate for medium with a case of a medium with soft layer only extending 10 km and a case of soft layer extending full length. (Simulation parameters: black curve: $H_1 = R$, $H_2 = 2R$, $H_3 = 10$ km, $H_4 = 10$ km, material contrast = 20 per cent, $R = 1.2$ km, $S = 1.0$; red curve: $H_1 = R$, $H_2 = 2R$, $H_3 = 90$ km, $H_4 = 10$ km, material contrast = 20 per cent, $R = 1.2$ km, $S = 1.0$.)

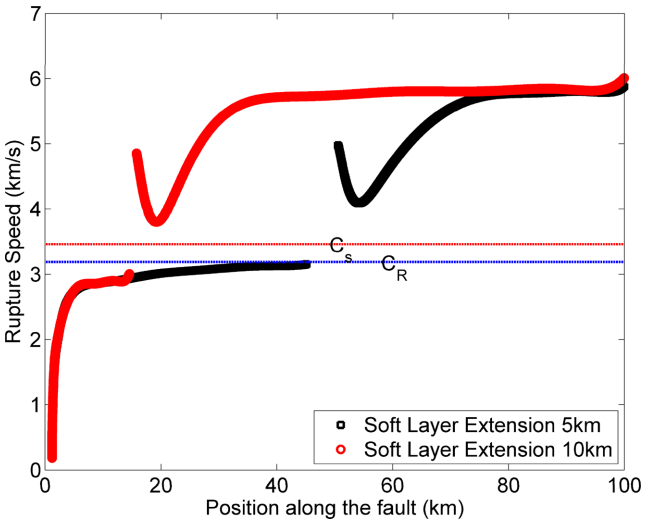

Figure 12. Variation of rupture speed for a medium with soft layers extending 5 and 10 km. The transition length to supershear has increased from 14.5 to 45.13 km as the soft layer extension is reduced from 10 to 5 km (as indicated by the position of the jumps in the rupture speed profile). c_s represents the shear wave speed and c_R represents the Rayleigh wave speed. (Simulation parameters: black curve: $H_1 = R$, $H_2 = 2R$, $H_3 = 5$ km, $H_4 = 10$ km, material contrast = 20 per cent, $R = 1.2$ km, $S = 1.0$; red curve: $H_1 = R$, $H_2 = 2R$, $H_3 = 10$ km, $H_4 = 10$ km, material contrast = 20 per cent, $R = 1.2$ km, $S = 1.0$.)

(14.55 km). Nonetheless, this value of the transition length is still smaller than the corresponding value for the homogeneous medium. This confirms our speculation that the reduction in transition length to supershear due to the soft inclusion becomes insensitive to the inclusion length only if the inclusion extends beyond a certain critical value. It also suggests that the presence of an inclusion with a length shorter than this value may still have an effect, albeit not as strong, on the supershear dynamics.

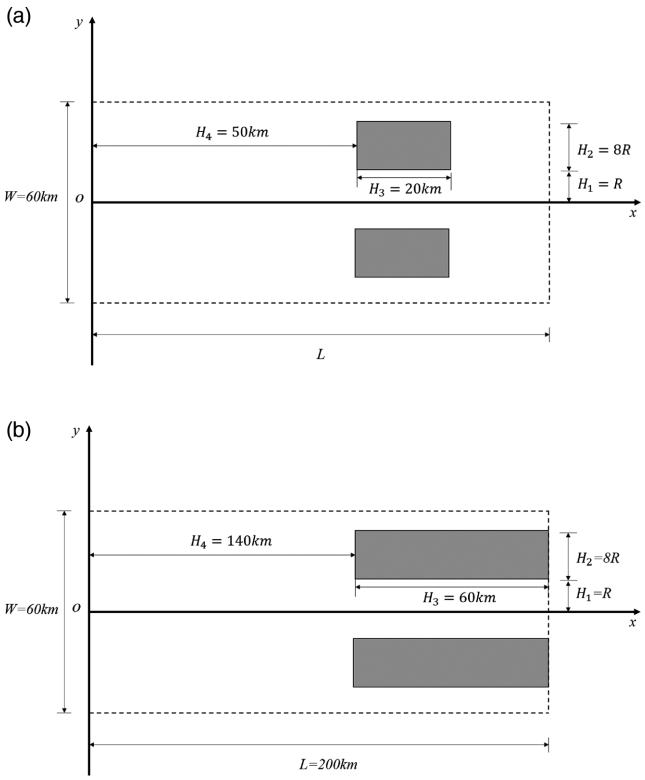

Figure 13. Layout of the soft inclusion with supershear rupture transitions at low stress level, the grey patch indicates the location of the inclusions. (a) Inclusion located from 50 to 70 km (simulation parameters: $H_1 = R$, $H_2 = 8R$, $H_3 = 20$ km, $H_4 = 50$ km, material contrast = 20 per cent, $R = 1.2$ km, $S = 2.0$); (b) inclusion located at 140–200 km (simulation parameters: $H_1 = R$, $H_2 = 8R$, $H_3 = 60$ km, $H_4 = 140$ km, material contrast = 20 per cent, $R = 1.2$ km, $S = 2.5$).

3.5 Supershear transition in understressed faults: effect of soft layer position

In this section, we investigate the effect of stress level ratio S on supershear transition characteristics. The limiting value of strength parameter S for supershear rupture to occur in homogeneous 2-D elastic media is 1.77. The existence of a soft layer violates the assumption of medium homogeneity and introduces additional interfaces for wave reflection and refraction. In this case, the limiting S value may be different from the homogeneous medium, and it may be even non-existent. Indeed, Huang *et al.* (2014) showed that the existence of LVZ adjacent to the fault surface enhances the supershear transition mechanism. Here, we present a few examples showing that rupture may transition into supershear under stress values that are lower than the limiting case predicted theoretically for the homogeneous media. This may be particularly relevant to faults existing in the vicinity of low-velocity sedimentary basins.

We investigate the possibility of supershear transition under uniformly lower pre-stress levels in the presences of a soft inclusion. For this purpose, we carry out simulations with the soft layer extending for a limited length parallel to the fault. We consider a velocity reduction value of 20 per cent. We find that it is possible to generate supershear rupture even if the strength parameter is uniform and equal to 2 along the fault length by positioning the soft inclusion at 50–70 km with width equal to $8R$ (Fig. 13a) .The supershear transition length is 56.3 km and the supershear is sustained as the rupture propagates beyond the soft layer area. In another geometry (Fig. 13b), we use a strength parameter $S = 2.5$, for a soft inclusion

extending from 140 to 200 km. Supershear rupture is observed with supershear transition length of 143.4 km. For 0 per cent velocity reduction (homogeneous medium), the transition length is predicted theoretically to be infinite. We thus hypothesize that in the presence of an off-fault soft layer, supershear may still happen under low stress levels if the layer is placed in a "favourable" position. A possible mechanism is the reflections from the soft layer to the fault surface enhance the building up of the shear stress ahead of the rupture front, and eventually lead to the nucleation of the daughter crack through the Burridge–Andrews mechanism.

If the rigidity of the soft layer approaches zero, it may be taken as an analogue of a free surface. Supershear transition due to free surface has been investigated for strike-slip faults by Kaneko & Lapusta (2010). Our observations suggest that supershear transition may occur at arbitrary low pre-stress values if a free surface exists parallel to the rupture propagation direction such as in some cases of normal faults and shallow parts of subduction zones. In order to study the effect of material contrast on supershear rupture transition, we conduct simulations with higher material contrast up to 40 and 60 per cent in Appendix C. We discuss the implications of this particular observation on rupture propagation on normal fault flats as well as the strike-slip faults in Section 4.

4 DISCUSSION

Identifying conditions under which supershear transition may occur during earthquake propagation is crucial for the development of a better understanding of earthquake physics as well as the estimation of ground motions and seismic hazard models. Supershear ruptures tend to be more destructive since the resulting waves travel longer distances with less attenuation than in their sub-shear counterparts (Dunham & Archuleta 2004). Heterogeneities in the Earth's crust are manifested in different forms. These include heterogeneities in the pre-stress, material properties, and friction laws. Exploring the interplay between different sources of heterogeneities and the dynamics of the rupture process is essential for the development of more realistic rupture models.

In this paper, we explored the influence of the existence of an off-fault material heterogeneity, represented by a low-velocity lens, on the rupture dynamics on a slip-weakening frictional interface. Our primary focus is on its effects on transition to supershear. Previous studies focused on other sources of heterogeneities such as variations in the pre-stress (Lapusta & Liu 2009) or fracture energy (Dunham *et al.* 2003). Our investigation is similar to Harris & Day (1997), Huang & Ampuero (2011), and Huang *et al.* (2014), where the authors explored the influence of an LVZ adjacent to the fault surface. A point of departure for our approach is that we allow the low-velocity layer to be placed at a finite distance from the fault surface. Moreover, the LVZ may be present in the form of a velocity anomaly within a limited region and need not extend throughout the length of the domain.

Velocity structure in the upper crust is generally heterogeneous (SCEDC 2013). It is most natural to think of LVZs as present in the immediate vicinity of pre-existing faults as a result of the damage caused by previous earthquakes. However, there may be situations in which the LVZ exists near but not immediately adjacent to the fault surface. Examples include (i) faults in the shallow parts of the crust near sedimentary basins and (ii) a member of a fault network in which the damaged zone adjacent to a nearby fault has lower rigidity than the damage zone in its immediate vicinity. Moreover, recent developments in the unified velocity structure models (SCEDC 2013) show that spatially heterogeneous velocity structure is more common than what was originally thought. With increased resolution and better detection methods, we will be able to identify more fine scale variations in this heterogeneous structure.

Different friction models have been developed to describe the evolution of fault strength. These include the slip-weakening models (Ida 1972; Palmer & Rice 1973; Uenishi & Rice 2003), the rate and state friction (Dieterich 1979; Ruina 1983), and the shear transformation zone theory (Daub & Carlson 2010; Elbanna & Carlson 2014; Lieou *et al.* 2014a,b). Rate-dependent models such as the Deterich–Ruina formulation or shear transformation zone friction models capture the evolution in fault strength in response to velocity changes and naturally account for healing as the slip rate is reduced. These features have important implications for rupture mode classification (Zheng & Rice 1998; Ampuero & Ben-Zion 2008). Linear slip-weakening models, on the other hand, do not naturally allow for fault healing and are insensitive to rate effects. Nonetheless, it is possible to map the parameters of slip-weakening friction to the corresponding parameters in the logarithmic rate and state law (Lapusta & Liu 2009). Thus, the results of the current study, derived based on linear slip-weakening friction, are expected to hold, at least qualitatively, if a more sophisticated logarithmic rate and state description is used.

The dynamic friction used in this study is equal to 0.5. This leads to a reasonable value of static stress drop ($\sim$2.5 MPa) (Allmann & Shearer 2009). However, this is relatively high compared to the expected strength level for mature faults. Due to the heat flow anomaly and lack of evidence for melting on mature faults (Sibson 1973; Lachenbruch 1980; Rice 2006), the actual value for dynamic friction is expected to be as low as 0.1 or 0.2. Several mechanisms have been proposed to account for the ultra-low dynamic friction including flash heating (Rice 2006; Beeler *et al.* 2008), pore fluid pressurization (Rice 2006; Noda & Lapusta 2010), silica gel formation (Goldsby 2002; Di Toro *et al.* 2004; Rice 2006), and nanoparticle lubrication (Han *et al.* 2011). We thus expect the heat generation associated with our friction model to be high and possibly consistent only with slip on dry and less mature faults (Di Toro *et al.* 2006) where traces of pseudotachylytes have been documented. We appreciate, however, that the rapid transition from high static friction to low dynamic friction is important for enabling rupture propagation in relatively low pre-stress conditions (Noda *et al.* 2011). The details of this transition has direct implications for the rupture mode classification and generation of self-healing slip pulses (Heaton 1990; Noda *et al.* 2009). We plan to extend this study to account for strong rate weakening friction in future investigations.

In this study, we nucleated the rupture abruptly by overstressing a region of the fault beyond its static frictional strength. This artificial nucleation leads to the rupture propagating dynamically from the beginning. This is different from the more natural quasistatic nucleation of real earthquakes. However, it is not rare that an earthquake may be triggered dynamically due to waves emitted from another earthquake (Brodsky 2006; Felzer & Brodsky 2006; Van der Elst *et al.* 2010). In this case, the nucleation will not be quasistatic. Moreover, this procedure is routinely used in generating laboratory earthquakes (Xu *et al.* 2009). Different nucleation protocols may affect the subsequent rupture propagation. In this paper, we used the same nucleation procedure as well as the same nucleation parameters in all the simulations. Thus, the artefacts that may be produced by the abrupt rupture initiation is common to all the results, and any observed variations may be attributed to changes in the other model parameters such as the soft layer thickness, off-fault distance, or material contrast.

The operation of most mature faults under overall low pre-stress (Noda *et al.* 2011) poses a paradox for supershear ruptures. On one hand, analytical and computational models predict that a relatively high pre-stress value ($S < 1.77$) is required for supershear transition to occur within a finite distance on slip-weakening frictional faults in 2-D homogeneous elastic media (Dunham 2007). Meanwhile, if supershear rupture propagation occurs on a mature fault, it must then occur at a much lower pre-stress. A possible resolution to this paradox includes the existence of favourable heterogeneities in the fault pre-stress (Lapusta & Liu 2009), heterogeneities in the fracture energy (Dunham 2007), or the existence of an LVZ adjacent to rate and state frictional fault (Huang *et al.* 2014). Here, we present an additional mechanism which is the existence of off-fault soft heterogeneities. The reflection of waves from the near-side boundary of the off-fault low-velocity region enhances the supershear transition and leads to the building up of stresses ahead of the rupture tip at a much lower background stress. We showed that as the velocity contrast between the inclusion and the background medium increases (Appendix C), the supearshear transition length decreases. Moreover, we report supershear propagation at pre-stress values corresponding to $S > 1.77$. This may suggest that the velocity structure near the fault surface plays an important role in determining the rupture propagation speed. Accounting for these heterogeneities will give more insight into conditions for supershear transition beyond what is possible from homogeneous models or heterogeneities limited to the fault surface only.

If the elastic moduli of the soft layer are taken to zero in the limit, the soft layer near-side boundary will approach the free surface condition. We observe that the transition length decreases as the material contrast between the soft layer and the background layer increases. Moreover, we show that as the material contrast increases, the pre-stress value at which supershear propagation becomes possible decreases. The existence of a free surface parallel to the rupture strike may enable supershear transition at much lower pre-stress values than what is predicted for the full space case. This situation is relevant to rupture propagation along flat portions in normal faults as well as propagation along the shallow parts of subduction zones. Moreover, the presence of asymmetric inclusions, such as a single nearby free surface, dynamic normal stress change will occur along the fault, changing the frictional strength and thus influencing the supershear transition. We plan to investigate this topic further in future studies.

In this paper, we consider a uniform stress outside the nucleation zone. The presence of the inclusion is expected to alter the stress state locally even if the far-field loading is uniform (Eshelby 1957; Burgmann *et al.* 1994). In particular, a low-velocity inclusion may create an area of low stress on the fault section within its extension. This understressing condition may counteract the wavefield enhancement created by the low-velocity layer, modify the frictional strength along the fault, and may delay or inhibit the supershear transition. Our results, so far, suggest that for the material contrast values considered in this paper the supershear transition continues to happen even in the presence of low stress area. We show an example of this calculation in Appendix D. The effect of stress heterogeneity on the supershear rupture dynamics is a topic of further research.

Future extension of this study may include the consideration of more realistic friction constitutive models such as rate and state friction with enhanced coseismic weakening, modelling the existence of off-fault stiff inclusions and representing more complex off-fault velocity structure. These investigations will also have implications for engineered composite materials in which the heterogeneous structure modulates the effective fracture toughness (Hossain *et al.* 2014).

5 CONCLUSION

We have analysed the supershear transition induced by an off-fault LVZ using simulations of spontaneous dynamic rupture on a fault governed by a linear slip-weakening friction law embedded in 2-D elastic medium. We have analysed factors that control the transition length to supershear rupture including the thickness of the soft layer, the contrast in the wave velocity between the soft inclusion and the rest of the domain, the stress level on the fault, and the length and position of the soft layer. We have shown that:

1. For the same pre-stress value, the transition to supershear rupture may occur at much smaller distances due to the existence of the soft inclusion.
2. For the same material contrast, the transition length decreases with the increase of the soft layer thickness (at a fixed off-fault distance) but increases with the increase of the distance between the layer and fault plane (at a fixed soft layer thickness).
3. The maximum reduction in the transition length happens if the soft layer extends to a distance that is slightly larger than the transition length value predicted for a soft layer that has the same length as the fault. That is, the extension of the soft layer beyond this value has a negligible effect on the transition length.
4. Supershear propagation may happen at a much lower pre-stress in the existence of an off-fault soft layer inclusion with limited length and width. However, the transition length diverges with the increase of the strength parameter S.

ACKNOWLEDGEMENTS

The authors are grateful to Ruth Harris, Jean-Paul Ampuero, Chen Ji and Yihe Huang for insightful discussions. A.E. Elbanna acknowledges support from the National Science Foundation NSF EAR1345108 as well as support from Southern California Earthquake Center through a collaborative agreement between NSF. Grant Number: EAR0529922 and USGS. Grant Number: 07HQAG0008.

REFERENCES

Aagaard, B.T., Kientz, S., Knepley, M., Strand, L. & Williams, C., 2013. *PyLith User Manual, Version 2.0.0*, Computational Infrastructure of Geodynamics.

Aki, K. & Richards, P.G., 2002. *Quantitative Seismology*, University Science Books.

Allmann, B. & Shearer, P., 2009. Global variations of stress drop for moderate to large earthquakes, *J. geophys. Res.*, **114**(B1), doi:10.1029/2008JB005821.

Ampuero, J.P. & Ben-Zion, Y., 2008. Cracks, pulses and macroscopic asymmetry of dynamic rupture on a bimaterial interface with velocity-weakening friction, *Geophys. J. Int.,* **173**(2), 674–692.

Andrews, D.J., 1976. Rupture velocity of plane strain shear cracks, *J. geophys. Res.,* **81**(32), 5679–5687.

Archuleta, R.J., 1984. A faulting model for the 1979 Imperial Valley earthquake, *J. geophys. Res.,* **89**(B6), 4559–4585.

Archuleta, R.J. & Day, S.M., 1980. Dynamic rupture in a layered medium: the 1966 Parkfield earthquake, *Bull. seism. Soc. Am.,* **70**(3), 671–689.

Beeler, N.M., Tullis, T.E. & Goldsby, D.L., 2008. Constitutive relationships and physical basis of fault strength due to flash heating, *J. geophys. Res.,* **113**(B1), doi:10.1029/2007JB004988.

Ben-Zion, Y. & Huang, Y., 2002. Dynamic rupture on an interface between a compliant fault zone layer and a stiffer surrounding solid, *J. geophys. Res.,* **107**(B2), 2042, doi: 10.1029/2001JB000254.

Ben-Zion, Y. *et al.*, 2003. A shallow fault-zone structure illuminated by trapped waves in the Karadere–Duzce branch of the North Anatolian Fault, western Turkey, *Geophys. J. Int.,* **152**(3), 699–717.

Ben-Zion, Y. & Sammis, C.G., 2003. Characterization of fault zones, *Pure appl. Geophys.,* **160**(3–4), 677–715.

Bizzarri, A., 2012. Formulation of a fault governing law at high sliding speeds: inferences from dynamic rupture models, *Earth planet. Sci. Lett.,* **355–356,** 223–230.

Bizzarri, A. & Das, S., 2012. Mechanics of 3-D shear cracks between Rayleigh and shear wave rupture speeds, *Earth planet. Sci. Lett.,* **357–358,** 397–404.

Bouchon, M. & Vallée, M., 2003. Observation of long supershear rupture during the magnitude 8.1 Kunlunshan earthquake, *Science,* **301**(5634), 824–826.

Bouchon, M., Toksöz, N., Karabulut, H., Bouin, M., Dietrich, M., Aktar, M. & Edie, M., 2000. Seismic imaging of the 1999 Izmit (Turkey) rupture inferred from the near-fault recordings, *Geophys. Res. Lett.,* **27**(18), 3013–3016.

Bouchon, M., Bouin, M., Karabulut, H., Toksöz, M.N., Dietrich, M. & Rosakis, A.J., 2001. How fast is rupture during an earthquake? New insights from the 1999 Turkey earthquakes, *Geophys. Res. Lett.,* **28**(14), 2723–2726.

Brodsky, E., 2006. Long-range triggered earthquakes that continue after the wave train passes, *Geophys. Res. Lett.,* **33**(15), doi:10.1029/2006GL026605.

Burgmann, R., Pollard, D.D. & Martel, S.J., 1994. Slip distributions on faults: effects of stress gradients, inelastic deformation, heterogeneous host-rock stiffness, and fault interaction, *J. Struct. Geol.,* **16**(12), 1675–1690.

Burridge, R., 1973. Admissible speeds for plane-strain self-similar shear cracks with friction but lacking cohesion, *Geophys. J. Int.,* **35**(4), 439–455.

Celebi, M. *et al.*, 2004. Near-field ground motion of the 2002 denali fault, Alaska, earthquake recorded at pump station 10, *Earthq. Spectra,* **20**(3), 597–615.

Cochran, E.S., Li, Y., Shearer, P.M., Barbot, S., Fialko, Y. & Vidale, J.E., 2009. Seismic and geodetic evidence for extensive, long-lived fault damage zones, *Geology,* **37**(4), 315–318.

Das, S. & Aki, K., 1977. A numerical study of two-dimensional spontaneous rupture propagation, *Geophys. J. Int.,* **50**(3), 643–668.

Daub, E. & Carlson, J., 2010. Friction, fracture, and earthquakes, *Annu. Rev. Condens. Matter Phys.,* **1**(1), 397–418.

Daub, E.G., Manning, M.L. & Carlson, J.M., 2010. Pulse-like, crack-like, and supershear earthquake ruptures with shear strain localization, *J. geophys. Res.,* **115**(B5), B05311, doi:10.1029/2009JB006388.

Day, S.M., 1982. 3-dimensional simulation of spontaneous rupture - the effect of nonuniform prestress, *Bull. seism. Soc. Am.,* **72**(6), 1881–1902.

Di Toro, G., Goldsby, D.L. & Tullis, T.E., 2004. Friction falls towards zero in quartz rock as slip velocity approaches seismic rates, *Nature,* **427**(6973), 436–439.

Di Toro, G., Hirose, T., Nielsen, S., Pennacchioni, G. & Shimamoto, T., 2006. Natural and experimental evidence of melt lubrication of faults during earthquakes, *Science,* **311**(5761), 647–649.

Dieterich, J., 1979. Modeling of rock friction: 1. Experimental results and constitutive equations, *J. geophys. Res.,* **84**(NB5), 2161–2168.

Dunham, E.M., 2007. Conditions governing the occurrence of supershear ruptures under slip-weakening friction, *J. geophys. Res.,* **112**(B7), B07302, doi:10.1029/2006JB004717.

Dunham, E.M. & Archuleta, R.J., 2004. Evidence for a supershear transient during the 2002 Denali fault earthquake, *Bull. seism. Soc. Am.,* **94**(6B), S256–S268.

Dunham, E.M., Favreau, P. & Carlson, J.M., 2003. A supershear transition mechanism for cracks, *Science,* **299**(5612), 1557–1559.

Elbanna, A.E. & Carlson, J.M., 2014. A two-scale model for sheared fault gouge: competition between macroscopic disorder and local viscoplasticity, *J. geophys. Res.,* **119**(6), 4841–4859.

Elkhoury, J. & Knopoff, L., 2012. Dynamical model of faulting in two dimensions and self-healing of large fractures, *Phys. Rev. E,* **86**(6 Pt 2), 066118, doi:10.1103/PhysRevE.86.066118.

Eshelby, J.D., 1957. The determination of the elastic field of an ellipsoidal inclusion, and related problems, *Proc. R. Soc. Lond. A,* **241**(1226), 376–396.

Felzer, K.R. & Brodsky, E.E., 2006. Decay of aftershock density with distance indicates triggering by dynamic stress, *Nature,* **441**(7094), 735–738.

Festa, G. & Vilotte, J.P., 2006. Influence of the rupture initiation on the intersonic transition: crack-like versus pulse-like modes, *Geophys. Res. Lett.,* **33**(15), L15320, doi:10.1029/2006GL026378.

Freund, L.B., 1990. *Dynamic Fracture Mechanics*, Cambridge Univ. Press.

Fukuyama, E. & Olsen, K.B., 2002. A condition for super-shear rupture propagation in a heterogeneous stress field, *Pure appl. Geophys.,* **159**(9), 2047–2056.

Gabriel, A.A., Ampuero, J.P., Dalguer, L.A. & Mai, P.M., 2012. The transition of dynamic rupture styles in elastic media under velocity-weakening friction, *J. geophys. Res.,* **117**(B9), B09311, doi:10.1029/2012JB009468.

Goldsby, D.L., 2002. Low frictional strength of quartz rocks at subseismic slip rates, *Geophys. Res. Lett.,* **29**(17), doi:10.1029/2002GL015240.

Han, R., Hirose, T., Shimamoto, T., Lee, Y. & Ando, J., 2011. Granular nanoparticles lubricate faults during seismic slip, *Geology,* **39**(6), 599–602.

Harris, R.A. & Day, S.M., 1997. Effects of a low-velocity zone on a dynamic rupture, *Bull. seism. Soc. Am.,* **87**(5), 1267–1280.

Heaton, T.H., 1990. Evidence for and implications of self-healing pulses of slip in earthquake rupture, *Phys. Earth planet. Inter.,* **64**(1), 1–20.

Hossain, M.Z., Hsueh, C.J., Bourdin, B. & Bhattacharya, K., 2014. Effective toughness of heterogeneous media, *J. Mech. Phys. Solids,* **71,** 15–32.

Huang, Y. & Ampuero, J., 2011. Pulselike ruptures induced by low-velocity fault zones, *J. geophys. Res.,* **116**(B12), B12307, doi:10.1029/2011JB008684.

Huang, Y., Ampuero, J.-P. & Helmberger, D.V., 2014. Earthquake ruptures modulated by waves in damaged fault zones, *J. geophys. Res.,* **119**(4), 3133–3154.

Ida, Y., 1972. Cohesive force across the tip of a longitudinal-shear crack and Griffith's specific surface energy, *J. geophys. Res.,* **77**(20), 3796–3805.

Kaneko, Y. & Lapusta, N., 2010. Supershear transition due to a free surface in 3-D simulations of spontaneous dynamic rupture on vertical strike-slip faults, *Tectonophysics,* **493**(3–4), 272–284.

Konca, A.O., Leprince, S., Avouac, J. & Helmberger, D.V., 2010. Rupture process of the 1999 Mw 7.1 Duzce earthquake from joint analysis of SPOT, GPS, InSAR, strong-motion, and teleseismic data: a supershear rupture with variable rupture velocity, *Bull. seism. Soc. Am.,* **100**(1), 267–288.

Lachenbruch, A., 1980. Frictional heating, fluid pressure, and the resistance to fault motion, *J. geophys. Res.,* **85**(NB11), 6097–6112.

Langer, S., Olsen-Kettle, L. & Weatherley, D., 2012. Identification of supershear transition mechanisms due to material contrast at bimaterial faults, *Geophys. J. Int.,* **190**(2), 1169–1180.

Lapusta, N. & Liu, Y., 2009. Three-dimensional boundary integral modeling of spontaneous earthquake sequences and aseismic slip, *J. geophys. Res.,* **114**(B9), doi:10.1029/2008JB005934.

Le Goff, A., Cobelli, P. & Lagubeau, G., 2013. Supershear Rayleigh waves at a soft interface, *Phys. Rev. Lett.,* **110**(23), 236101, doi:10.1103/PhysRevLett.110.236101.

Lewis, M.A. & Ben-Zion, Y., 2010. Diversity of fault zone damage and trapping structures in the Parkfield section of the San Andreas Fault from comprehensive analysis of near fault seismograms, *Geophys. J. Int.,* **183**(3), 1579–1595.

Lewis, M.A., Peng, Z., Ben-Zion, Y. & Vernon, F.L., 2005. Shallow seismic trapping structure in the San Jacinto fault zone near Anza, California, *Geophys. J. Int.,* **162**(3), 867–881.

Li, H., Zhu, L. & Yang, H., 2007. High-resolution structures of the Landers fault zone inferred from aftershock waveform data, *Geophys. J. Int.,* **171**(3), 1295–1307.

Li, Y., Aki, K., Adams, D., Hasemi, A. & Lee, W.H.K., 1994. Seismic guided waves trapped in the fault zone of the Landers, California, earthquake of 1992, *J. geophys. Res.,* **99**(B6), 11 705–11 722.

Li, Y., Chen, P., Cochran, E.S., Vidale, J.E. & Burdette, T., 2006. Seismic evidence for rock damage and healing on the San Andreas fault associated with the 2004 M 6.0 Parkfield earthquake, *Bull. seism. Soc. Am.,* **96**(4B), S349–S363.

Li, Y., Vidale, J.E., Day, S.M., Oglesby, D.D. & the SCEC Field Working Team, 2002. Study of the 1999 M 7.1 Hector Mine, California, earthquake fault plane by trapped waves, *Bull. seism. Soc. Am.,* **92**(4), 1318–1332.

Li, Y.G. & Leary, P.C., 1990. Fault zone trapped seismic waves, *Bull. seism. Soc. Am.,* **80**(5), 1245–1271.

Lieou, C.K.C., Elbanna, A. & Carlson, J.M. 2014a. Grain fragmentation in sheared granular flow: weakening effects, energy dissipation, and strain localization, *Phys. Rev. E,* **89**(2), doi:10.1103/PhysRevE.89.022203.

Lieou, C.K.C., Elbanna, A., Langer, J.S. & Carlson, J.M., 2014b. Shear flow of angular grains: acoustic effects and nonmonotonic rate dependence of volume, *Phys. Rev. E,* **90**(3), doi:10.1103/PhysRevE.90.032204.

Liu, Y. & Lapusta, N., 2008. Transition of mode II cracks from sub-Rayleigh to intersonic speeds in the presence of favorable heterogeneity, *J. Mech. Phys. Solids,* **56**(1), 25–50.

Madariaga, R. & Olsen, K.B., 2000. Criticality of rupture dynamics in 3-D, *Pure appl. Geophys.,* **157**(11–12), 1981–2001.

Mizuno, T., Kuwahara, Y., Ito, H. & Nishigami, K., 2008. Spatial variations in fault-zone structure along the Nojima fault, Central Japan, as inferred from borehole observations of fault-zone trapped waves, *Bull. seism. Soc. Am.,* **98**(2), 558–570.

Noda, H., Dunham, E.M. & Rice, J.R., 2009. Earthquake ruptures with thermal weakening and the operation of major faults at low overall stress levels, *J. geophys. Res.,* **114**(B7), B07302, doi:10.1029/2008JB006143.

Noda, H., Kanagawa, K., Hirose, T. & Inoue, A., 2011. Frictional experiments of dolerite at intermediate slip rates with controlled temperature: rate weakening or temperature weakening?, *J. geophys. Res.,* **116**(B7), B07306, doi:10.1029/2010JB007945.

Noda, H. & Lapusta, N., 2010. Three-dimensional earthquake sequence simulations with evolving temperature and pore pressure due to shear heating: effect of heterogeneous hydraulic diffusivity, *J. geophys. Res.,* **115**(B12), doi:10.1029/2010JB007780.

Oglesby, D.D., Mai, P.M., Atakan, K. & Pucci, S., 2008. Dynamic models of earthquakes on the North Anatolian fault zone under the sea of Marmara: effect of hypocenter location, *Geophys. Res. Lett.,* **35**(18), doi:10.1029/2008GL035037.

Payne, R.M. & Duan, B., 2015. Influence of initial stress and rupture initiation parameters on forbidden zone rupture propagation, *Geophys. J. Int.,* **201**(1), 70–77.

Palmer, A.C. & Rice, J.R. 1973. The growth of slip surfaces in the progressive failure of over-consolidated clay, *Proc. R. Soc. A,* **332**(1591), 527–548.

Peng, Z., Ben-Zion, Y., Michael, A.J. & Zhu, L., 2003. Quantitative analysis of seismic fault zone waves in the rupture zone of the 1992 Landers, California, earthquake: evidence for a shallow trapping structure, *Geophys. J. Int.,* **155**(3), 1021–1041.

Rice, J., 2006. Heating and weakening of faults during earthquake slip, *J. geophys. Res.,* **111**(B5), doi:10.1029/2005JB004006.

Robinson, D.P., Brough, C. & Das, S., 2006. The Mw 7.8, 2001 Kunlunshan earthquake: extreme rupture speed variability and effect of fault geometry, *J. geophys. Res.,* **111**(B8), B08303, doi:10.1029/2005JB004137.

Ruina, A., 1983. Slip instability and state variable friction laws, *J. geophys. Res.,* **88**(B12), 10359–10370.

Ryan, K.J. & Oglesby, D.D., 2014. Dynamically modeling fault step overs using various friction laws, *J. geophys. Res.,* **119**(7), 5814–5829.

SCEDC, 2013. *Southern california earthquake center*. Caltech.Dataset. doi:10.7909/C3WD3xH1.

Shi, Z., Ben Zion, Y. & Needleman, A., 2008. Properties of dynamic rupture and energy partition in a solid with a frictional interface, *J. Mech. Phys. Solids,* **56**(1), 5–24.

Sibson, R., 1973. Interactions between temperature and pore-fluid pressure during earthquake faulting and a mechanism for partial or total stress relief, *Nat. Phys. Sci.,* **243**(126), 66–68.

Spudich, P. & Cranswick, E., 1984. Direct observation of rupture propagation during the 1979 imperial valley earthquake using a short baseline accelerometer array, *Bull. seism. Soc. Am.,* **74**(6), 2083–2114.

Tape, Carl, 2009. Seismic tomography of southern California using adjoint methods, *PhD thesis*, California Institute of Technology.

Uenishi, K. & Rice, J., 2003. Universal nucleation length for slip-weakening rupture instability under nonuniform fault loading, *J. geophys. Res.,* **108**(B1), 2042, doi:10.1029/2001JB001681.

Vallée, M., Landès, M., Shapiro, N.M. & Klinger, Y., 2008. The 14 November 2001 Kokoxili (Tibet) earthquake: high-frequency seismic radiation originating from the transitions between sub-Rayleigh and supershear rupture velocity regimes, *J. geophys. Res.,* **113**(B7), B07305, doi:10.1029/2007JB005520.

Van der Elst, N.J., Brodsky, E. & Brodsky, E.E., 2010. Connecting near-field and far-field earthquake triggering to dynamic strain, *J. geophys. Res.*, **115**(B7), doi:10.1029/2009JB006681.

Walker, K.T. & Shearer, P.M., 2009. Illuminating the near-sonic rupture velocities of the intracontinental Kokoxili Mw 7.8 and Denali fault Mw 7.9 strike-slip earthquakes with global *P* wave back projection imaging, *J. geophys. Res.,* **114**(B2), B02304, doi:10.1029/2008JB005738.

Xu, C. *et al.*, 2009. Identification and analysis of secondary geological hazards triggered by a magnitude 8.0 Wenchuan earthquake, *J. Romote Sens.,* **13**(4), 754–762.

Yang, H. & Zhu, L., 2010. Shallow low-velocity zone of the San Jacinto fault from local earthquake waveform modelling, *Geophys. J. Int.,* **183**(1), 421–432.

Yang, H., Zhu, L. & Cochran, E.S., 2011. Seismic structures of the Calico fault zone inferred from local earthquake travel time modelling, *Geophys. J. Int.,* **186**(2), 760–770.

Zhan, Z., Helmberger, D., Kanamori, H. & Shearer, P., 2014. Supershear rupture in a Mw 6.7 aftershock of the 2013 Sea of Okhotsk earthquake, *Science,* **345**(6193), 204–207.

Zheng, G. & Rice, J., 1998. Conditions under which velocity-weakening friction allows a self-healing versus a cracklike mode of rupture, *Bull. seism. Soc. Am.,* **88**(6), 1466–1483.

APPENDIX A: MESH CONVERGENCE STUDY

We test the convergence of the numerical solutions by conducting simulations on two meshes with 25 and 12.5 m element size. We show in Fig. A1 a snapshot of the slip rate computed on the two

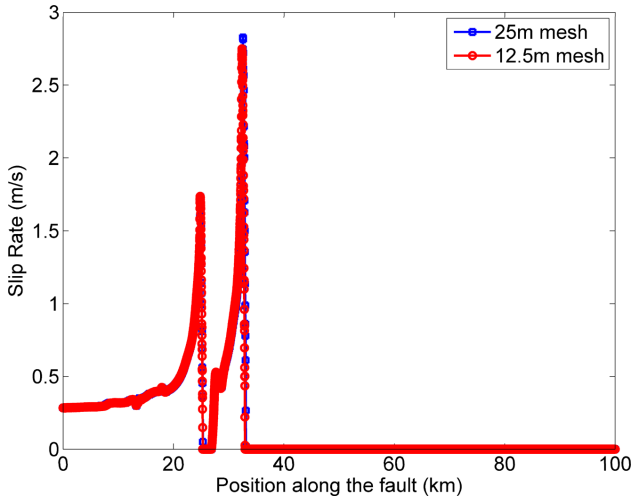

Figure A1. Snapshot for slip rate on the fault surface for 25 and 12.5 m mesh sizes. (Simulation parameters: $H_1 = R$, $H_2 = 2R$, $H_3 = 100$ km, $H_4 = 10$ km, $R = 1.2$ km.)

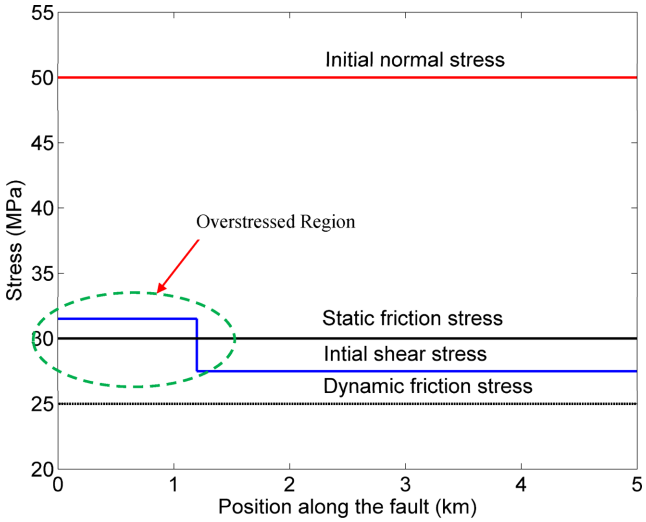

Figure B1. The initial shear stress distribution along the fault. Nucleate the rupture by overstressing the region from 0 to R with initial shear stress 31.0 MPa, with $R = 1.2$ km, keep the normal stress as a constant along the fault.

meshes corresponding to the case with 20 per cent material contrast, strength parameter $S = 1$, and soft inclusion parameters $H_1 = \mathrm{R}$, $H_2 = 2R$, $H_3 = 20$ km, $H_4 = 10$ km. The results are indistinguishable. Furthermore, the process zone (the zone extending from the peak slip rate to the rupture tip) is well resolved with numerous elements in both cases (22 elements on the 25 m grid and 44 elements on the 12.5 m grid). All simulations presented in this study are based on the 25 m grid.

APPENDIX B: NUCLEATION PROCEDURE

In this paper, we conduct all the simulations under the same nucleation procedure. As shown in Fig. B1, we overstress the region from 0 to R which $R = 1.2$ km calculated from Eq. (2). The initial shear stress is uniform everywhere except in the overstressed region where it is elevated to 31 MPa, a value that is slightly higher than the static frictional strength (30 MPa). Fig. B1 shows the different stress levels corresponding to strength parameter $S = 1.0$.

APPENDIX C: DEPENDENCE OF SUPERSHEAR TRANSITION ON VELOCITY CONTRAST

Here, we investigate the impact of the material contrast between the background domain and the soft inclusion on the supershear transition. We conduct simulations with material contrast 40 and 60 per cent. Although this high contrast values may not be extensive in the earth, there is some evidence that the local velocity variations in fault zones may reach these high values (Huang & Ampuero 2011). All the simulations are conducted with the soft inclusion starting from 10 km and extending to the end. As shown in Fig. C1, for a fault with low stress levels ($S = 2$, $S = 2.5$), the supershear transition length becomes smaller as the material contrast increase. This is because the amplitude of the reflected waves from the near-side boundary of the soft inclusion increases as the material contrast increases (Fig. C2). The continuous reflections from the soft layer to the fault surface enhance the building up of the shear stress ahead of the rupture front, and eventually lead to the earlier nucleation of the daughter crack through the Burridge–Andrews mechanism.

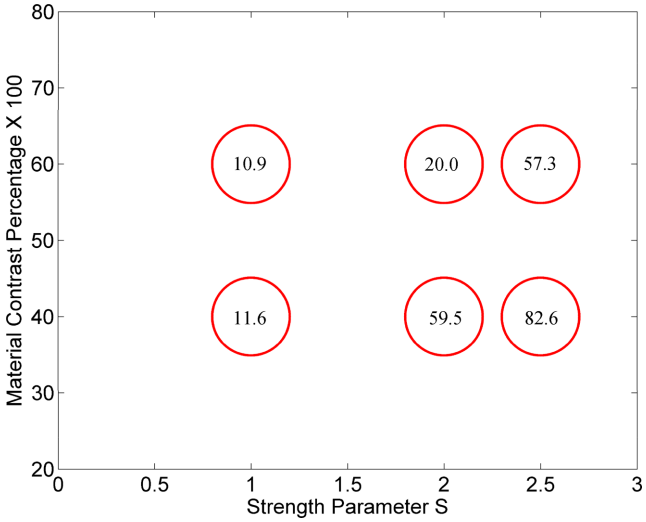

Figure C1 . Values of transition length (in km) with respect to material contrast and strength parameter S. The values in the red circle are results from simulation of the soft inclusion starting from 10 km extending to the end of the domain. (Simulation parameters: $H_1 = R$, $H_2 = 2R$, $H_3 = 90$ km, $H_4 = 10$ km, $R = 1.2$ km.)

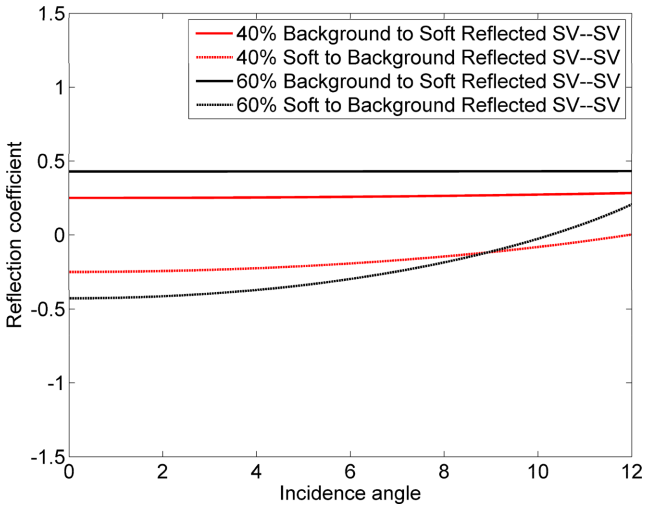

Figure C2. Reflection coeficient for incidient SV waves at boundary between background medium and soft layer with velcoity reduction of 40 and 60 per cent, both the reflection coefficent from the soft inclusion to the background medium and from the background medium to the soft inclusion are shown in the figure. The reflected SV waves are considered. The incident angle of SV waves are plotted below the first critical angle. The phase is zero for this range of incident angles. Formulas of relection coefficients are taken from Aki & Richards (2002).

APPENDIX D: SUPERSHEAR TRANSITION IN THE PRESENCE OF LOW-STRESSED AREA INDUCED BY THE SOFT INCLUSION

A uniform far-field loading will generate uniform stresses in homogeneous medium. However, the stress state may be altered in the presence of inclusion. To test this hypothesis, we first compute the static stress field under uniform far-field shearing. We observe in this case that an area of low shear stress develops on the fault plane in the vicinity of the soft inclusion. To investigate the influence of this low stress area on supershear transition, we conduct a dynamic simulation with 20 per cent material contrast between the

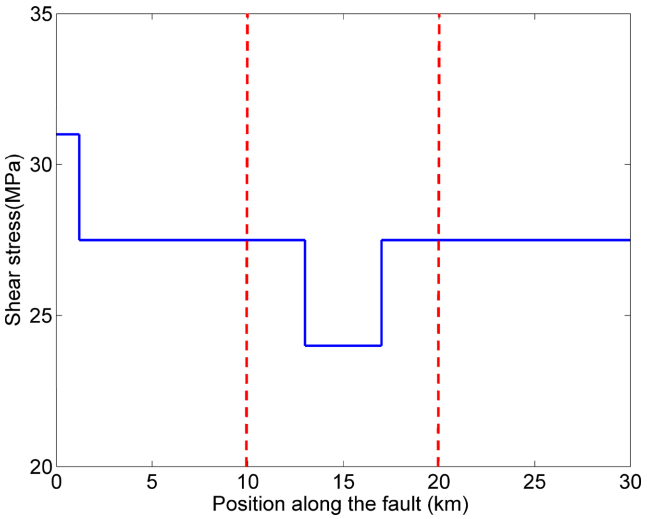

Figure D1. The initial shear stress distribution along the fault accounting for the effect of the soft inclusion. The rupture is nucleated by overstressing the region from 0 to $R = 1.2$ km with initial shear stress 31.0 MPa. The red dashed line indicates the location of the inclusion from 10 to 20 km. Within the region extending between 13 and 17 km the shear stress drops to 24 MPa. This leads to a strength parameter $S = -6$. In the rest of the fault, the shear stress is kept constant at the level of 27.5 MPa.

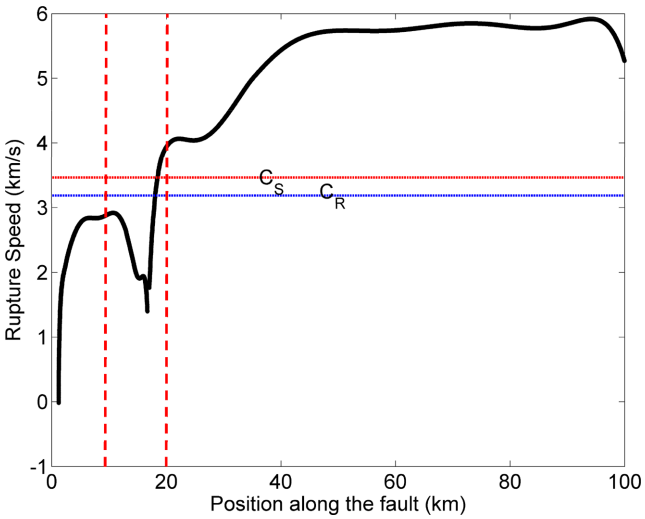

Figure D2. Variation of rupture speed for medium with soft layer inclusion with non-unifrom stress level on the fault surface. The red dashed line indicates the location of the soft inclusion. (Simulation parameters: $H_1 = R$, $H_2 = 2R$, $H_3 = 10$ km, $H_4 = 10$ km, material contrast = 20 per cent, $R = 1.2$ km, $S = 1.0$, except the low stress area; see Fig. D1.)

soft inclusion and the background medium (same material contrast used for the static problem), and parameters $H_1 = R$, $H_2 = 2R$, $H_3 = 20$ km, $H_4 = 10$ km. We use the same nucleation procedure as before with $R = 1.2$ km. However, we decrease the initial shear stress from 27.5 to 24 MPa within the region extending between 13 and 17 km consistent with what is observed in the static problem. The simulation result shows that even with the presence of the low stress area [$S = -6$], the initial shear stress is shown in Fig. D1, we still obtain supershear rupture, as shown in Fig. D2. This suggests that the wavefield enrichment due to the material contrast may overcome the effects of understressing. However, the simulations show that the supershear transition in this case does not occur through the Burridge-Andrews Mechanism. Rather, the rupture speed continuously pass through the 'energetically forbidden zone' bounded by the Rayleigh wave sped C_R and shear wave speed C_S. As shown in Fig. D2, there are sudden rupture deceleration (13 km) and rupture acceleration (17 km). The sudden changes in rupture speed may intensify the radiated field and influence the transition mechanism of the supershear rupture. The phenomenon of the rupture speed continuously passing through the 'energetically forbidden zone' will be a topic of further research.